

Temporal downflows in a penumbra

J. Jurčák¹ and Y. Katsukawa²

¹ Astronomical Institute of the Academy of Sciences, Fričova 298, 25165 Ondřejov, Czech Republic
e-mail: jurcak@asu.cas.cz

² National Astronomical Observatory of Japan, 2-21-1 Osawa, Mitaka, Tokyo 181-8588, Japan

Received 2 April 2010 / Accepted 25 June 2010

ABSTRACT

Aims. We analyze temporal downflow patches that are located in a penumbra and have the same polarity of the magnetic field as a sunspot umbra.

Methods. The repetitive 2'' wide raster scans of penumbral regions that are taken with one minute cadence by the Hinode spectropolarimeter are used to detect the line-of-sight velocities in the penumbra from enhanced signals in the wings of Stokes V profiles. The lifetimes and positions within penumbra of the identified downflow patches are investigated. The plasma properties of the downflow patches are determined using the inversions of the observed Stokes profiles.

Results. The temporal downflows have lifetimes of up to fourteen minutes. Some of them are related to the disappearance or weakening of nearby upflow regions or to the chromospheric brightenings. The downflows take place in regions with stronger and more vertical magnetic fields than the upflow regions.

Key words. Sun: sunspots – Sun: photosphere – Sun: chromosphere – techniques: polarimetric

1. Introduction

The velocity structure of the penumbra is dominated by the Evershed flow, i.e., a horizontal outflow discovered by Evershed (1909). With increasing spatial resolution, the fine structure of the flow pattern has been discovered in the past decade. It was found (see e.g., Rimmele & Marino 2006; Ichimoto et al. 2007, and references therein) that the Evershed flow starts with the upflow in bright penumbral grains and becomes horizontal within one arcsecond. Westendorp Plaza et al. (2001) found a downflow regions in the outer penumbra that have opposite magnetic field polarity than the sunspot umbra and suggested that these might be the sinks of the Evershed flow. This was supported by the findings of Ichimoto et al. (2007) and Franz & Schlichenmaier (2009) who analyzed data of higher spatial resolution.

The observed fine structure of the Evershed flow agrees with the theoretical model of the penumbral fine structure proposed by Schlichenmaier et al. (1998). This model predicts a magnetic flux tube that rises above the continuum formation layer and quickly becomes horizontal, a flow develops along this tube because of the gas pressure gradient. However, this model cannot describe the sink of the flux tube because of its simplicity and the adopted boundary conditions.

Another model proposed to explain the penumbral fine structure was suggested by Spruit & Scharmer (2006). This model proposes that the bright filaments are heated by convection occurring in field-free gaps just below the continuum formation layer. This model cannot explain the velocity structures observed in the penumbra. The weak-field gaps (or highly squeezed flux tubes) can be identified in the results of radiative MHD simulations of sunspot structure (Rempel et al. 2009b,a). The simulated maps of line-of-sight (LOS) velocity show downflow structures along the central upflow region created by the overturning convection. These downflows have yet to be confirmed by observations. Zakharov et al. (2008) found a weak downflow on the center-ward side of a filament structure where the upflow was

observed. However, the Milne-Eddington inversion used placed the strongest and most vertical magnetic field in the location of the downflow, which is inconsistent with the proposed overturning convection. More advanced inversion codes applied to similar observations (possibly for sunspots located at the disc center) are needed to confirm these findings. For details see the recent review by Schlichenmaier (2009).

In this paper, downflows that have the same polarity as the sunspot umbra are studied (hereafter called just downflows). These were identified by Katsukawa & Jurčák (2010) in a sunspot located close to the disc center. Since the penumbral magnetic field is strong enough, the flows must follow its orientation. Therefore, the downflows are observed only at the center-side penumbra where the field points towards the observer. These downflows have a patch-like structure. A higher number of identified events and the temporal evolution is discussed here.

2. Observations and data reduction

We study observations of the active region NOAA 10926 taken by the Solar Optical Telescope (SOT, Tsuneta et al. 2008) onboard the Hinode satellite (Kosugi et al. 2007). The active region was located at heliocentric position 10° S and across the range 2°–16° W on 2006 December 1 and 2.

The Hinode spectropolarimeter (SP) scanned a narrow region repetitively. The SP acquires all four Stokes profiles of two lines of neutral iron at 630.15 nm and 630.25 nm. The width of the spectrograph slit and the step of the slit is equivalent to 0'.16, the height of the spectrograph slit was 256 pixels, the exposure time was 4.8 s per slit position, and the raster scans consisted of 13 slit positions. Thus, the cadence of the scanning was approximately one minute and the scanned area was about 2'' wide and 41'' high. The resulting noise level is around $10^{-3}I_c$ and the spatial resolution 0'.32. On December 1, the observations were taken between 11 UT and 17 UT and there are 319 completed

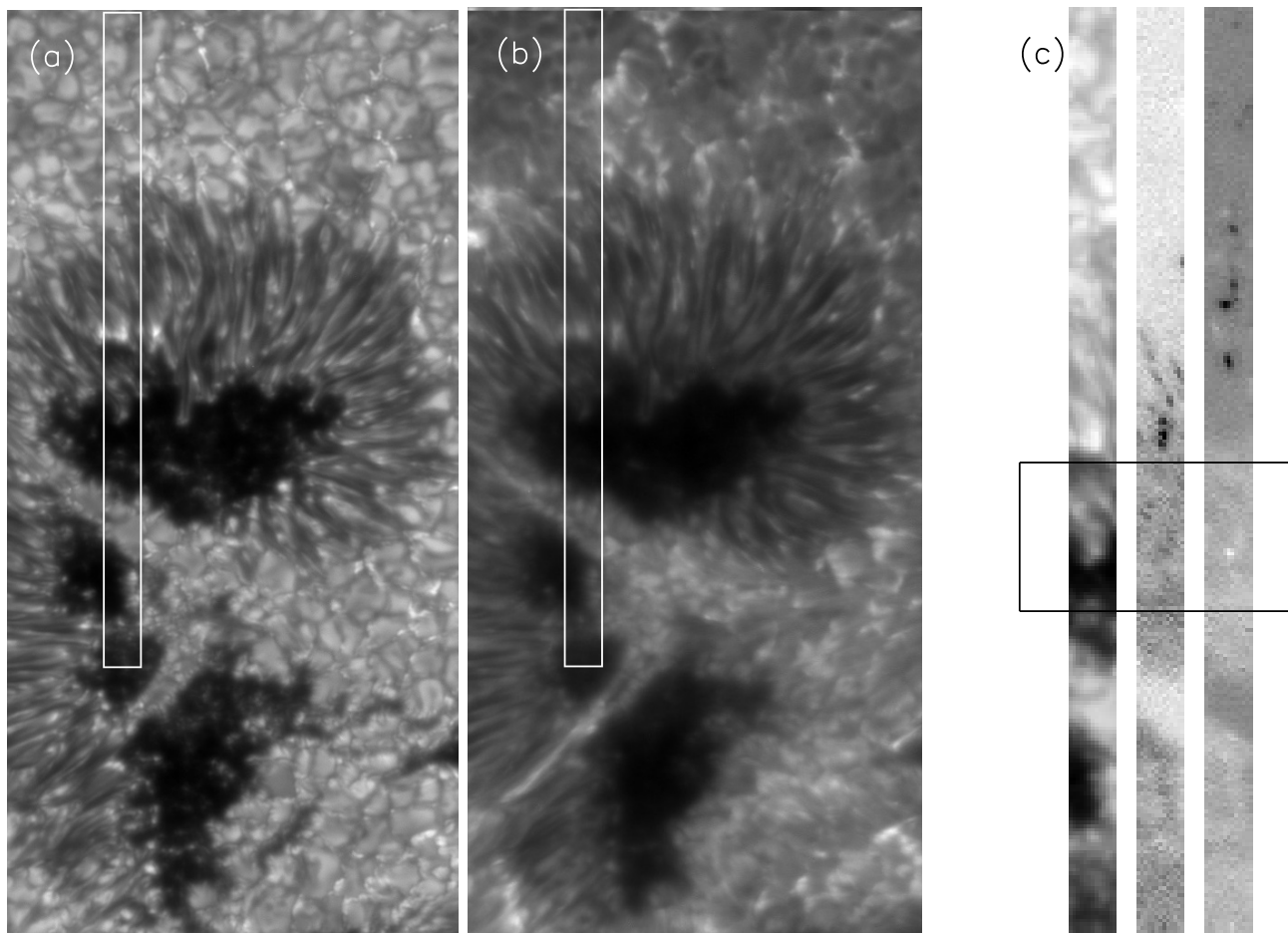


Fig. 1. The G-band **a**) and Ca II H **b**) images of part of the active region NOAA 10926. The white contours mark the area repetitively scanned by the SP. The intensities obtained from SP measurements are shown in **c**). From left to right: the continuum intensity around 630.3 nm (I_c) and the intensity in the blue and red wing of the Stokes V profile (-25.8 pm and $+25.8$ pm from the line center of the 630.15 nm line, respectively). The black contours in **c**) mark the region, whose evolution is depicted in Fig. 6b.

scans of the narrow region. On December 2, 267 scans were taken between 10:30 UT and 15:30 UT.

For comparison with the SP data, we also calibrated the filtergram (FG) observations taken through the G-band and Ca II H filters. The G-band data were used to co-align the FG and SP data, whereas the Ca II H images were used to determine the chromospheric activity above the penumbral downflows. Both the SP and FG data were calibrated with standard routines available in the Hinode SolarSoft package. The calibration of wavelengths, i.e., zero LOS velocity, was performed using the line center of an average quiet Sun profile. The convective blue-shift was not corrected.

In Figs. 1a and b, we show the G-band and Ca II H images of active region NOAA 10926. The marked area shows the region repetitively scanned by the SP. In Fig. 1c, we show the observed SP parameters (see the caption for details).

3. Identification of downflow patches

As demonstrated by Ichimoto et al. (2007), the enhanced signals in the far wings of the Stokes V profiles may be an indication of higher LOS velocities. The signals may be also enhanced by the increase in the magnetic field strength and (or) increase in temperature. However, these mechanisms enhance the intensities at both wings of the Stokes V profile. Therefore, enhanced signals

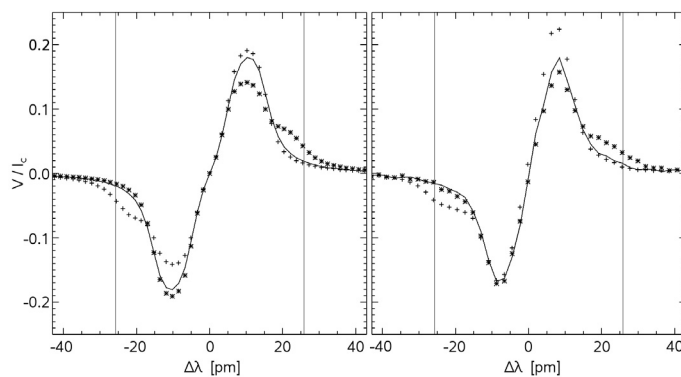


Fig. 2. The synthetic (*left*) and observed (*right*) Stokes V profiles of Fe I 630.15 nm line. The solid lines represent the atmosphere with low LOS velocity (set to zero at all heights in case of synthetic profile). The (+) symbols represent a profile with an upflow (negative LOS velocity); observed in a bright grain and synthesised with LOS velocity set to -2.5 km s^{-1} below $\log(\tau) = -0.3$. The (*) symbols represent the Stokes V profile with a positive LOS velocity; created with LOS velocity set to 2.5 km s^{-1} below $\log(\tau) = -0.3$ and observed in a downflow patch.

in only one wing clearly identify regions with an upflow or a downflow.

In the left part of Fig. 2, we show three synthetic profiles of the Fe I 630.15 nm line, which differ only in terms of the

stratification of LOS velocity. In the right part of Fig. 2, we show the Stokes V profiles observed in pixels with very low LOS velocity, in the bright grain, and in the downflow patch (see the caption for details).

The amplitudes and widths of the synthetic profiles were altered to roughly match the observed profiles. Therefore, the stratifications of temperature, magnetic field strength, and LOS velocity used do not correspond to those expected in the sunspot penumbra. But it is clear that the synthetic and observed Stokes V profiles have the same characteristics. The zero crossings of all the profiles are at almost the same wavelength, i.e., there are no differences in LOS velocity at higher layers of the line-forming region. The amplitude of the lobe with the enhanced signal at the far wing is also smaller than the second lobe and than the amplitude of the lobe resulting from the atmosphere with zero LOS velocity. This is not so obvious in the case of the observed profiles, but we have to keep in mind that although these profiles were observed in pixels close to each other, they have different stratifications of temperature and magnetic field strength.

The middle panel in Fig. 1c shows the intensities observed in the far blue wing of the Stokes V profile, -25.8 pm from the line center as marked by the thin vertical lines in Fig. 2. The dark patches in this panel correspond to profiles similar to the one observed in the bright grains with an upflow that is shown in Fig. 2. Thus, the dark patches correspond to areas of the same polarity as the sunspot umbra and flows towards the observer (upflows). The right panel in Fig. 1c shows the intensities observed in the far red wing. The white patch is created by Stokes profiles comparable to the one observed in the downflow patch shown in Fig. 2, i.e., in regions with the same polarity as the sunspot umbra and downflows. Dark patches are also seen in the right panel of Fig. 1c. That are in areas with downflows, but have the opposite magnetic field polarity to the sunspot umbra. As mentioned in Sect. 1, these areas are considered to be the sinks of the Evershed flow and are mostly located in the outer penumbra.

To identify the downflow patches, we have to examine the regions with enhanced positive signals in maps analogous to the right panel of Fig. 1c. Since the observed signals are also dependent on the temperature and magnetic field strength that are changing throughout the penumbra, no absolute threshold value can be specified. The differences between the observed signals and an average values observed at a given position within the penumbra are instead used to identify the downflow regions. The downflows identified have to occupy at least two neighboring pixels to avoid the mistaken identification of signals caused by the noise.

4. Results

4.1. Downflows statistics

In both analyzed datasets, there are 181 identified downflow patches. In Table 1, we show the numbers of all identified events (second column) with respect to their lifetimes (first column). The events last up to 14 min, the most frequent being downflows detected at two consecutive scans, i.e., lifetimes of between two and three minutes. From all the identified downflow patches, 25% appear or disappear at the edge of the FOV. The average lifetime inferred from all identified events is 3.46 scans. This value is not influenced significantly by the limited FOV, i.e., is approximately the same for events remaining in the FOV

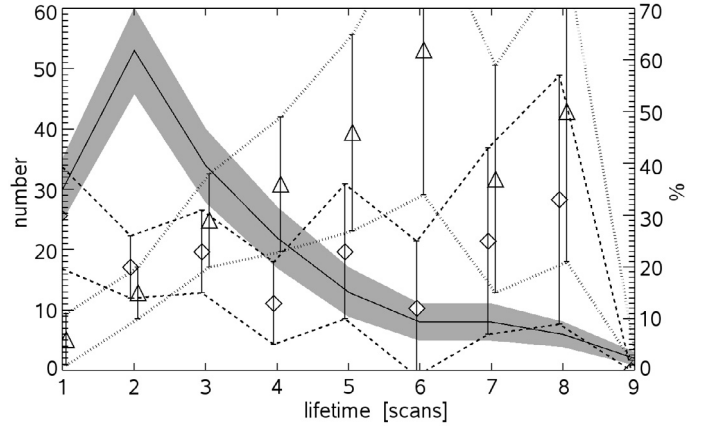


Fig. 3. The number of identified events is marked by a solid line and the shaded area indicates its uncertainty. The \diamond and \triangle symbols show the percentage of downflows that are related to chromospheric brightenings and nearby upflows, respectively. The uncertainties in these values are marked by dashed and dotted lines, respectively.

Table 1. Statistical properties of the downflows.

Lifetime [scans]	Identified Events	Related to Jets [%]	Related to Upflows [%]
1	30	30	6
2	53	20	15
3	34	23	29
4	22	13	36
5	13	23	46
6	8	12	62
7	8	25	37
8	6	33	50
9	2	0	0
11	1	0	100
12	1	100	0
14	3	0	33

for their whole lifetime and for events that move in or out of the FOV.

The minimal lifetime cannot be estimated from the datasets used since the time resolution of one minute is insufficient. The number of identified events smoothly decreases with increasing lifetime as shown by the solid line in Fig. 3. The shaded area indicates the uncertainties if we assume a Poisson distribution. The third and fourth columns of Table 1 as well as the other lines in Fig. 3 are discussed in Sect. 4.2.

In Fig. 4, we show the positions of identified downflows and upflows along the slit during the repetitive scanning of the narrow region. We can see the movements in the penumbra for the longer-lasting events. The upflow regions drift generally towards lower y values and this corresponds to the movement towards the sunspot umbra. However, there are also upflows that migrate in the opposite direction, towards the quiet Sun, which are located mostly in the outer penumbra. This is consistent with the findings of Sobotka et al. (1999) who studied the movements of bright penumbral grains related to the upflow structures (e.g., Rimmele & Marino 2006; Ichimoto et al. 2007). The downflow patches also drift in both directions with speeds comparable to those of the upflow regions. However, there are also downflows that drift more rapidly in both directions. The directions of these fast drifting downflows do not seem to be dependent on the position within penumbra.

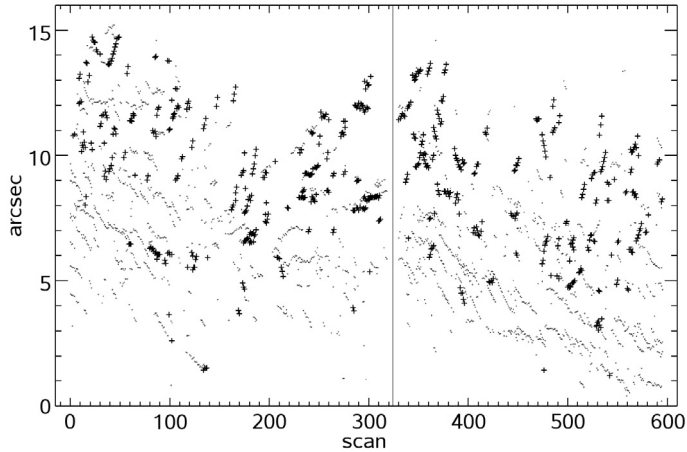


Fig. 4. Positions of identified upflow and downflow events along the SP slit (• and + symbols) evolving during the repetitive scanning. The thin vertical line separates the datasets obtained on 2006 December 1 and 2.

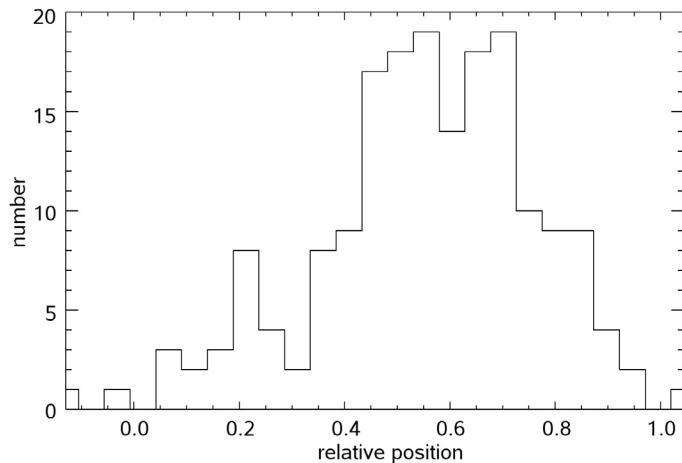


Fig. 5. Histogram of the mean positions of the identified downflow patches, where zero on the x axis correspond to the umbra/penumbra boundary and one to the penumbra/quiet Sun boundary.

From Fig. 4, it is also obvious that the downflow events have shorter lifetimes than the upflows. According to Sobotka et al. (1999), the lifetimes of penumbral bright grains are mostly around 20 min, where Table 1 shows that over 75% of identified downflows have lifetimes up to five minutes.

As can be seen in Fig. 4, the downflows are more often located in the outer penumbra. Using the estimated umbra/penumbra and penumbra/quiet Sun boundaries, the histogram of positions of identified downflows is plotted in Fig. 5. The mean position is used for the longer-lasting events, which might create uncertainties for the fast moving downflow patches. There is also a problem with the definition of the penumbral boundaries for this narrow region. However, it does not affect that the downflows mostly occur in the outer penumbra, between 0.4 and 0.8 where zero is the umbra/penumbra boundary and one is the penumbra/quiet Sun boundary.

4.2. Origin of the downflow patches

As suggested by Katsukawa et al. (2007) and Katsukawa & Jurčák (2010), the downflow patches might be related to the temporal chromospheric brightenings (penumbral micro-jets)

representing the downward oriented outflow from the reconnection site. The magnetic reconnection can occur between the horizontally oriented flux tubes surrounded by a stronger and more vertical component of the magnetic field (Solanki & Montavon 1993). The possibility of this reconnection was confirmed by simplistic simulations by Sakai & Smith (2008, 2009). Magara (2010) performed MHD simulations of a flux tube embedded in a stronger and more vertical magnetic field. This configuration is closer to that expected in the penumbra and also resulted in reconnection producing the outflows oriented upward and downward and following the stronger and more vertical component of the magnetic field (observationally found by Jurčák & Katsukawa 2008).

Using the FG observations through the Ca II H filter, the identified downflow patches can be compared to the chromospheric activities above them. This was performed manually and the tentative results are shown in the third column of Table 1 and in Fig. 3. On average, 22% of the identified downflows seem to be related to some chromospheric brightenings. From the number of analyzed events it is difficult to determine, if the probability is dependent on the lifetime of the downflows.

While comparing the downflows with the chromospheric activity, we noticed that some of the downflows are almost both spatially and temporarily coincident with the termination of upflow structures. This can be explained, if we assume that the configuration of the flux tube carrying the flow can be described by the simulations of Schlichenmaier et al. (1998) confirmed observationally by Rimmele & Marino (2006). If the flow in the filament were to weaken and the flux tube to collapse, then we would end up with hot material above the continuum formation layer that is no longer forced to follow the field lines of the flux tube. This hot material would cool down and fall back along magnetic field lines of possibly different strength and orientation creating a temporal downflow close to the former upflow region. Thus, the downflow would just be a consequence of the upflow termination, not the cause of it.

The relation between the downflows and upflows was again investigated manually and the results are shown in the fourth column of Table 1 and in Fig. 3. On average, 35% of the downflows occur close to the upflows and are possibly related to their termination. However, there is a dependence of this relation on the lifetime of the downflows. The peak value of 62% is reached for downflows that last for six scans (six minutes), but there are only eight events with this lifetime and the uncertainty is high. There are also four downflow patches that seem to precede the appearance of upflow region. However, all these events occur either in regions containing a number of upflow structures or near the edge of the FOV. For these reasons, it is generally not possible to align the upflows and downflows unambiguously.

There are only two downflows from the 181 identified that are related to both the chromospheric brightening and the termination of the upflow structure. More than 50% of the observed downflows do not seem to be related to any of the mechanisms that have been proposed to explain their origin. This percentage might be influenced by the narrow FOV in the case of the associated upflow structures that can occur out of it and by the insufficient temporal resolution of the Ca II H imaging that can miss the chromospheric brightenings with lifetimes shorter than one minute.

In Fig. 6, we show examples of individual downflows. From top to bottom, we illustrate a downflow patch related only to (a) the chromospheric brightening; (b) the termination of the upflow region; (c) both the chromospheric brightening and the

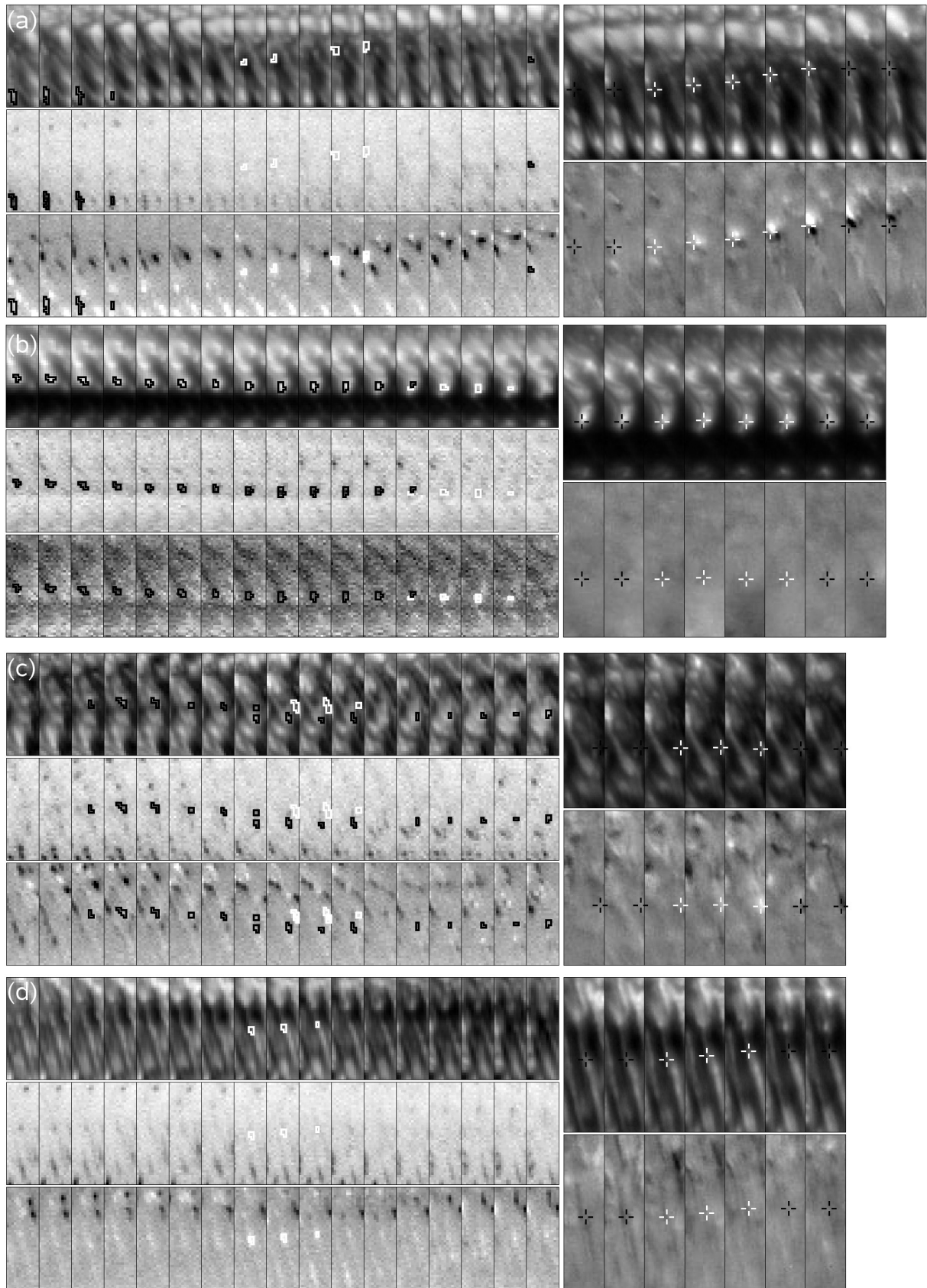


Fig. 6. In the left parts, we show the maps of intensities observed with SP analogous to those in Fig. 1c. The white contours mark the discussed downflow patches and the black contours mark the nearby upflow regions, i.e., not all velocity structures are marked by the contours. In the right parts, we show the maps of intensities of the same regions as scanned by the SP observed by FG. The top maps are the G-band intensities and the lower maps show the running difference of Ca II H images, i.e., the changes in the intensities of the chromosphere. The white crosses show the position of the downflow patch during its occurrence and the black crosses show its position before and after its lifetime. The four shown cases are discussed in the text.

Table 2. Plasma properties^a in the downflow patches and nearby upflow regions.

Event	N^D	N^U	I_c^D	I_c^U	I_c^{D-U}	v_{LOS}^D	v_{LOS}^U	v_{LOS}^{D-U}	γ^D	γ^U	γ^{D-U}	B^D	B^U	B^{D-U}
			[counts]				[km s ⁻¹]			[deg]			[G]	
1	2	21	20 200	23 450	-3250	0.57	-1.84	2.41	145	135	10	2000	1800	200
2	3	56	24 000	25 750	-1750	0.66	-1.58	2.24	140	130	10	1550	1280	270
3	7	72	23 900	27 000	-3100	0.61	-1.51	2.12	145	130	15	2050	1380	670
4	25	142	24 250	30 050	-5800	0.72	-1.91	2.63	135	120	15	1630	1180	450
5	1	32	27 500	28 700	-1200	0.61	-1.69	2.30	125	120	5	990	1020	-30
6	13	41	29 000	28 300	700	0.98	-1.65	2.63	125	120	5	1480	1080	400
7	2	30	27 200	28 800	-1600	0.72	-1.68	2.40	125	120	5	1150	1000	150
8	6	5	27 400	28 700	-1300	0.90	-1.61	2.51	130	125	5	1210	1160	50
					-2175			2.405			9.4			265

Notes. ^(a) For individual events, we list absolute values of continuum intensity, LOS velocity, magnetic field inclination, and magnetic field strength in the downflow patch (upper index D) and in the nearby upflow region (upper index U) and also the difference in these values (upper index D-U). The values of plasma parameters are averaged in the range of optical depths between $\log(\tau) = -0.2$ and -0.4 . The last line shows the average differences between the downflow and upflow regions. The second and third columns show the number of pixels used to derive the characteristic values in the downflow and upflow regions, respectively.

termination of the upflow region; and (d) not related to any of these two events (see the caption for details).

In Figs. 6a and c, we show the downflows related to penumbral brightenings. These are just slightly elongated and do not resemble the penumbral micro-jets observed by Katsukawa et al. (2007). As shown by Jurčák & Katsukawa (2008), the penumbral micro-jets follow the orientation of the magnetic field and in the observed part of the penumbra, the field basically points towards the observer. Therefore, we observe more patch-like structures than jets (as also discussed in Katsukawa & Jurčák 2010). In both of the illustrated cases, the chromospheric brightening is observed approximately two minutes after the downflow appears. In most of the observed cases, the downflow is similarly observed before the brightening appears in the chromosphere. This delay supports the findings of Katsukawa & Jurčák (2010) who concluded that if the chromospheric brightenings and the downflows are caused by the reconnection, then the reconnection occurs in the photospheric layers.

In Figs. 6b and c, we show typical examples of downflows related to the termination of nearby upflow regions. In the case of Fig. 6b, the downflow occurred in a filament that protruded deeply into the sunspot umbra. This can be seen in Fig. 1 since the black contours in Fig. 1c mark the region whose evolution is shown in Fig. 6b. There are no other flows in the nearby area that would complicate the interpretation of this particular event. The upflow can be traced back to scans that occurred previously to those shown in Fig. 6b. It is observed in a total of 18 scans (minutes), before that it is out of the FOV. In one scan, we observe both the upflow and the downflow, and the downflow lasts for another three scans. In 11 scans after that, neither upflows nor downflows are observed in the discussed bright grain before the remnant of it leaves the FOV.

All other downflows related to the termination of the upflow region occur in the penumbra, where a number of flow structures can be observed. In the case of Fig. 6c, the downflow observed in three scans terminates the upflow region lasting on a previous six scans. In the scan where the downflow appears, there are no black contours marking the upflow, but enhanced negative signals can still be seen in the middle left panel of Fig. 6c. The signal is just not strong enough to exceed the threshold used in the algorithm for the automatic detection. The number of nearby upflows (middle left panel) and downflows (with both polarities, lower left panel) observed inside the penumbra make it difficult

to relate the downflows to the disappearance of the upflows. The closest upflow that appears in a bright grain a few pixels lower is marked by black contours, but it is probably not related to the discussed events.

In Fig. 6d, we show the most typical example of the downflow patch. There is neither any nearby upflow region nor any changes in the chromospheric intensity around the identified downflow structure.

4.3. Plasma properties in the downflow patches

We also attempted to estimate the plasma properties in the downflow patches using the inversion code SIR (Stokes Inversion based on Response function, Ruiz Cobo & del Toro Iniesta 1992). A similar investigation was performed by Katsukawa & Jurčák (2010). Here we used a slightly different setup of the inversion code of four nodes for temperature and LOS velocity, five nodes for magnetic field strength, three nodes for inclination, and one node for magnetic field azimuth and microturbulent velocity. We used only one-component model of atmosphere to keep the number of free parameters at a reasonable value, but the observed downflows are mostly smaller than the spatial resolution of the Hinode SP. The local polarized straylight can to some extent compensate for the unresolved component, but it could not be used in this case because of the narrow FOV. We tried several attempts of inversions with two-component model of atmosphere, but the resulting fits were not as good as those obtained with the one-component model.

We considered only the downflow patches related to the disappearance of upflow regions and compared the resulting plasma parameters between these structures. We were unable to perform the inversion for the whole dataset because of its size, and only several downflows were selected. In Table 2, we summarize the resulting values for eight of these downflows. The presented values of plasma parameters represent the average obtained in the range of optical depths between $\log(\tau) = -0.2$ and -0.4 . As mentioned before, the flow structures and especially the downflows are not resolved and the inversion scheme used does not account for this. Therefore, we used only pixels, where the resulting values of LOS velocity exceed 0.5 km s^{-1} and -1 km s^{-1} for downflows and upflows, respectively. The numbers of these pixels for a given event are shown in the second and third columns of Table 2 for downflow and upflow patches,

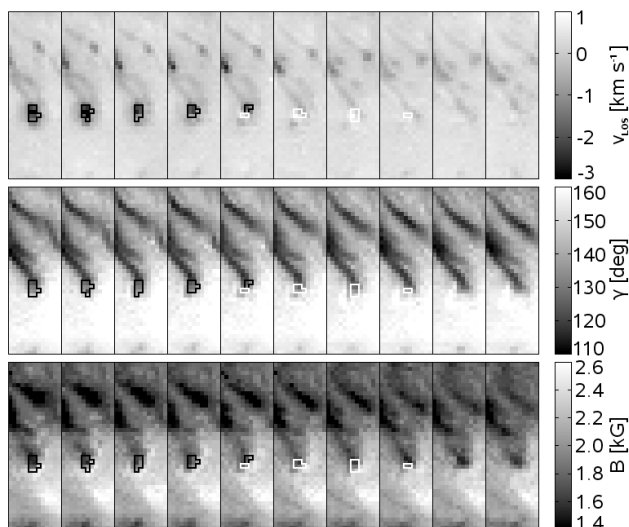


Fig. 7. Maps of resulting values of plasma parameters averaged in the range of optical depths between $\log(\tau) = -0.2$ and -0.4 . From top to bottom, we show the LOS velocity, inclination of the magnetic field, and magnetic field strength. The area shown corresponds to the one shown in Fig. 6b.

respectively. These pixels correspond to the central parts of the patches and a one-component model of atmosphere is more reasonable there.

The downflow patches are usually found in darker regions of the penumbra than the upflow structures. The magnetic field is stronger and more vertical in the downflow patches compared to the nearby upflow regions by on average 265 G and 9.4° . In Fig. 7, we show maps of the resulting plasma parameters for the event displayed in Fig. 6b. This event is also listed in Table 2 as number 1 and we can see that the inversion code found strong downflows at only two pixels during the evolution of this downflow patch.

The upflow velocities in the penumbral bright grains are larger than those reported by Rimmele & Marino (2006, around 1 km s^{-1}) and comparable to those reported by Sobotka & Jurčák (2009, between $1\text{--}2 \text{ km s}^{-1}$), but still smaller than the theoretically predicted 3 km s^{-1} from the magnetic-flux-tube model by Schlichenmaier et al. (1998). The magnetic field strength in the upflow regions is comparable to the values reported by Sobotka & Jurčák (2009) for penumbral bright grains and also to values found for the inner penumbra by e.g., Jurčák et al. (2007), Borrero et al. (2006), and Bellot Rubio et al. (2004). The agreement with previous results make the simplified inversion trustworthy at least for the upflow structures that are spatially larger than the downflow patches. However, the obtained values of the plasma parameters in the downflow patches cannot be compared to any previous results since these were only studied by Katsukawa & Jurčák (2010), where the inversion method was analogous to the one used for this analysis.

5. Conclusions

Following the discovery of penumbral downflows of the same polarity as the sunspot umbra by Katsukawa & Jurčák (2010), we have used the Hinode SP data that allow us to study the temporal behavior of these structures. In total, we have identified 181 downflow patches with lifetimes mostly around two or three minutes. The maximal lifetime is 14 min, while the shortest cannot be estimated because of the insufficient temporal resolution

of the data used. These downflows occur mostly in the outer penumbra and their horizontal velocities are comparable to or higher than those of penumbral bright grains.

As found out by Katsukawa & Jurčák (2010), we confirm that some of the downflows seem to be related to chromospheric brightenings. However, this connection is found only for around 20% of all identified events. This relation can be explained by the reconnection process, where the chromospheric brightening represents the upward oriented outflow (no velocity information for these chromospheric brightenings has ever been obtained) and the temporal downflow is the downward oriented outflow. From the observed Stokes V profiles, it is obvious that the flow occurs in the lower layers of the line-forming region and that in higher atmospheric layers the LOS velocity is close to zero. This means that the reconnection process takes place in the middle or lower photospheric layers, which is consistent with the observed time delay between the downflow patch appearance and the beginning of chromospheric brightening. This photospheric reconnection was demonstrated to be possible by theoretical simulations by Sakai & Smith (2008, 2009) and Magara (2010).

We have proposed another mechanism to explain the origin of the downflow patches. Some of the downflows are related to the disappearance of nearby upflow regions. This relation is dependent on the lifetime of the downflows with maximum of 62% reached for downflows lasting for about 6 min. By assuming that the hot material above the continuum-forming layer created by the upflow is no longer forced to follow the field lines (becoming an horizontal outflow, Rimmele & Marino 2006), it would radiatively cool down and fall back creating a temporal downflow. This explanation is supported by the difference in the continuum intensity within both the upflow regions and the downflow patches, the latter occurring in darker regions. The results of the inversion have shown that the downflows occur in regions with more vertical and stronger magnetic field than the upflow regions. This might indicate that the flux tube with a weaker and more horizontal magnetic field that carried the upflow has been destroyed and that the previously hot material falls along field lines that are more vertical. This mechanism assumes the uncombined configuration of the magnetic field proposed by Solanki & Montavon (1993).

More than 50% of the observed downflows do not seem to be related to any of these two mechanisms. This might be related to the insufficient temporal resolution of the Ca II H imaging and narrow FOV of the SP measurements. On the other hand, there are only two downflows that are related to both the chromospheric brightening and the termination of the nearby upflow region. Supposing that the reconnection between the magnetic field lines of the flux tube and the surrounding magnetic field terminates the flux tube, one can expect a higher number of downflows to be related to both of the proposed mechanism simultaneously. However, if the reconnection does not take place right next to the penumbral bright grain (where the upflow takes place) but further along the flux tube, then the upflow structure is not co-spatial with the chromospheric brightening and the downflow patch would not be related to both of these mechanisms. A more detailed analysis of these structures is necessary. However, there are currently no instruments that can provide us with data of significantly higher quality required for this type of analysis.

Acknowledgements. The support from GA AS CR IAA 300030808 is gratefully acknowledged. Hinode is a Japanese mission developed and launched by ISAS/JAXA, with NAOJ as domestic partner and NASA and STFC (UK) as

international partners. It is operated by these agencies in cooperation with ESA and NSC (Norway).

References

- Bellot Rubio, L. R., Balthasar, H., & Collados, M. 2004, *A&A*, 427, 319
- Borrero, J. M., Solanki, S. K., Lagg, A., Socas-Navarro, H., & Lites, B. 2006, *A&A*, 450, 383
- Evershed, J. 1909, *MNRAS*, 69, 454
- Franz, M., & Schlichenmaier, R. 2009, *A&A*, 508, 1453
- Ichimoto, K., Shine, R. A., Lites, B., et al. 2007, *PASJ*, 59, 593
- Jurčák, J., & Katsukawa, Y. 2008, *A&A*, 488, L33
- Jurčák, J., Bellot Rubio, L., Ichimoto, K., et al. 2007, *PASJ*, 59, 601
- Katsukawa, Y., & Jurčák, J. 2010, *A&A*, 524, A20
- Katsukawa, Y., Berger, T. E., Ichimoto, K., et al. 2007, *Science*, 318, 1594
- Kosugi, T., Matsuzaki, K., Sakao, T., et al. 2007, *Sol. Phys.*, 243, 3
- Magara, T. 2010, *ApJ*, 715, L40
- Rempel, M., Schüssler, M., Cameron, R. H., & Knölker, M. 2009a, *Science*, 325, 171
- Rempel, M., Schüssler, M., & Knölker, M. 2009b, *ApJ*, 691, 640
- Rimmele, T., & Marino, J. 2006, *ApJ*, 646, 593
- Ruiz Cobo, B., & del Toro Iniesta, J. C. 1992, *ApJ*, 398, 375
- Sakai, J. I., & Smith, P. D. 2008, *ApJ*, 687, L127
- Sakai, J. I., & Smith, P. D. 2009, *ApJ*, 691, L45
- Schlichenmaier, R. 2009, *Space Sci. Rev.*, 144, 213
- Schlichenmaier, R., Jahn, K., & Schmidt, H. U. 1998, *A&A*, 337, 897
- Sobotka, M., & Jurčák, J. 2009, *ApJ*, 694, 1080
- Sobotka, M., Brandt, P. N., & Simon, G. W. 1999, *A&A*, 348, 621
- Solanki, S. K., & Montavon, C. A. P. 1993, *A&A*, 275, 283
- Spruit, H. C., & Scharmer, G. B. 2006, *A&A*, 447, 343
- Tsuneta, S., Ichimoto, K., Katsukawa, Y., et al. 2008, *Sol. Phys.*, 249, 167
- Westendorp Plaza, C., del Toro Iniesta, J. C., Ruiz Cobo, B., & Pillet, V. M. 2001, *ApJ*, 547, 1148
- Zakharov, V., Hirzberger, J., Riethmüller, T. L., Solanki, S. K., & Kobel, P. 2008, *A&A*, 488, L17